JACS
JOURNAL OF THE AMERICAN CHEMICAL SOCIETY
Article
pubs.acs.org/JACS

Bonding, Ion Mobility, and Rate-Limiting Steps in Deintercalation Reactions with $ThCr_2Si_2$-type KNi_2Se_2

James R. Neilson and Tyrel M. McQueen*

Department of Chemistry and Department of Physics and Astronomy, The Johns Hopkins University, Baltimore, Maryland 21218, United States

Supporting Information

ABSTRACT: Here, we study the nature of metal−metal bonding in the $ThCr_2Si_2$ structure type by probing the rate-limiting steps in the oxidative deintercalation of KNi_2Se_2. For low extents of oxidation, alkali ions are removed exclusively to form $K_{1-x}Ni_2Se_2$. For greater extents of oxidation, the rate of the reaction decreases dramatically, concomitant with the extraction of both potassium and nickel to form $K_{1-x}Ni_{2-y}Se_2$. The appreciable mobility of transition metal ions is unexpected, but illustrates the relative energy scales of different defects in the $ThCr_2Si_2$ structure type. Furthermore, the fully oxidized compounds, $K_{0.25}Ni_{1.5}Se_2$, spontaneously convert from the tetrahedral $[NiSe_4]$-containing $ThCr_2Si_2$ structure to a vacancy-ordered NiAs structure with $[NiSe_6]$ octahedra. From analysis of the atom positions and kinetic data, we have determined that this transformation occurs by a continuous, low-energy pathway via subtle displacements of Ni atoms and buckling of the Se sublattice. These results have profound implications for our understanding of the stability, mobility, and reactivity of ions in materials.

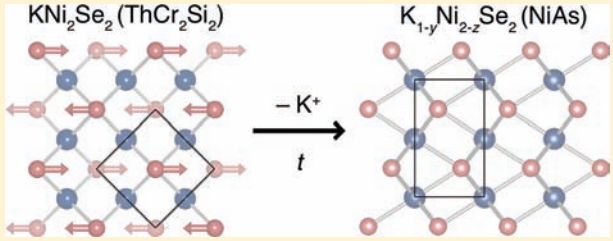

INTRODUCTION

Oxidative deintercalation chemistry finds utility in many applications, from batteries to the synthesis of novel metastable compounds with interesting magnetic or electronic properties. When electrochemically driven, these reactions are useful for storing energy, since reductive intercalation reactions with Li^+ often yield electronic currents with driving potentials in excess of 3 V.[1,2] Traditional low-temperature *chimie douce* (soft chemistry) solution reactions are typically used to synthesize novel compounds.[3,4] The chemical deintercalation of alkali metals from host lattices with I_2 or Br_2 has been particularly successful in tuning the composition, structure, and magnetic properties of myriad materials,[5−8] including the discovery of numerous new superconducting materials, $Na_{0.35}CoO_2{\cdot}1.3\ H_2O$[9] and the Chevrel phases $A_xMo_6(S/Se)_8$.[10,11] In the case of the Chevrel phases, the nature of bonding (i.e., the electronic structure) has been extensively probed by electrochemical variation of the electron count[5,12,13] and by molecular-orbital theory and band structure calculations.[14]

Here, we demonstrate control of the oxidative deintercalation of KNi_2Se_2 to $K_{1-x}Ni_2Se_2$ and $K_{1-y}Ni_{2-z}Se_2$ by selectively targeting the oxidation and deintercalation steps with separate reagents. KNi_2Se_2 is built of two-dimensional layers of edge-sharing $[NiSe_4]$ tetrahedra separated by alkali ions (Figure 2),[15] and has a purple/red luster and an unusual formal oxidation state of $Ni^{1.5+}$. Oxidative hole-doping of KNi_2Se_2 does not yield exotic magnetic properties, but the chemical reactivity of the oxidative deintercalation reactions reveals tremendous insight into the key mechanistic steps of these reactions and the nature of defect chemistry of KNi_2Se_2 and related $ThCr_2Si_2$-type compounds. In addition, our results revealed an unexpected structural relationship between the canonical $ThCr_2Si_2$ and NiAs structure types.

With low oxidant concentrations, solely potassium is extracted from KNi_2Se_2, with a 0.20(3) eV activation barrier for the rate limiting step, the solid-state diffusion of potassium. However, at high oxidant concentrations, the rate of the reaction decreases dramatically, and chemical analysis shows this slow-down is concomitant with the extraction of both potassium and nickel ions. Furthermore, the oxidized phases spontaneously transform at room temperature to a structure resembling that of NiAs, a structure built of face-sharing $[NiSe_6]$ octahedra. This transformation nucleates and grows by way of small displacements of nickel atoms and buckling of the selenium sublattice. The reaction mechanisms of both oxidative deintercalation and the $ThCr_2Si_2$-to-NiAs structural transformation are explained in terms of electron count and Ni−Ni bonding. These results provide great insight into controlling the chemistry of *chimie douce* reactions, defect chemistry in structurally analogous iron-based superconductors, and rate-limiting mechanisms in oxidative deintercalation reactions.

RESULTS

Rietveld analysis of high-resolution synchrotron powder X-ray diffraction (Figure 1, Table 1) confirms the previously reported composition and structure of the starting material, KNi_2Se_2.[15] There are no weak supercell peaks or other signs of additional

Received: December 23, 2011
Published: April 24, 2012

   dx.doi.org/10.1021/ja212012k | J. Am. Chem. Soc. 2012, 134, 7750−7757

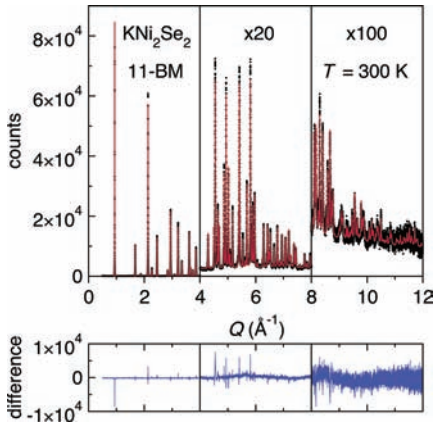

Figure 1. Rietveld analysis of high-resolution synchrotron X-ray diffraction data of KNi_2Se_2 showing the data (black dots), calculated profile (red line), and their difference (blue line). At higher Q, the y-axes are scaled by ×20 (4−8 Å^{-1}) and ×100 (8−12 Å^{-1}) to highlight the quality of the fit across all Q.

Table 1. Structure Parameters of KNi_2Se_2 Determined by High-Resolution Synchrotron X-ray Diffraction[a]

site	x	y	z	occ	U_{11}[b]	U_{33}[b]
K	0	0	0	1	1.24(2)	2.33(4)
Ni	0	0.5	0.25	1	1.103(8)	2.50(2)
Se	0	0	0.35429(2)	1	0.916(5)	2.17(1)

[a]Space group: $I4/mmm$, lattice parameters error constrained from laboratory X-ray diffraction with an internal Si standard: a = 3.9089(8), c = 13.4142(5). Goodness-of-fit given by: χ^2 = 2.92, R_{wp} = 7.26%, R_p = 6.28%. [b]Thermal parameters multiplied by 100.

structural periodicities. The refined site occupancies do not deviate from the ideal KNi_2Se_2 stoichiometry within 2%, and thus were fixed at unity in the final refinement.

The oxidative deintercalation of potassium from KNi_2Se_2 to $K_{1-x}Ni_2Se_2$ is easily afforded by $[Cu^{2+} + 2I^-]$ in acetonitrile at room temperature. For reactions with low amounts of oxidant, $x < 0.25$ with x = mol $[Cu^{2+} + 2I^-]$/mol KNi_2Se_2, completion of the reaction is clearly denoted by the transparency of the supernatant: Cu^+ is colorless, while Cu^{2+} is strongly amber/brown. However, for reactions with $x \geq 0.25$, the supernatant retains a faint yellow hue even after long equilibration times. X-ray diffraction of the reaction products (plotted on a logarithmic y axis in Figure 2) reveals no trace of secondary oxidation products (e.g., elemental Se) and retention of the $I4/mmm$ symmetry of KNi_2Se_2, with only subtle differences in Bragg peak positions and intensities.

The X-ray diffraction data collected on the reaction products (Figure 2) reveals single-phase products for $x < 0.25$ and $x > 0.9$. A two-phase region exists for $0.25 \leq x \leq 0.90$; the inhomogeneous products comprise two phases with distinct lattice parameters and $I4/mmm$ symmetry. Since the Bragg reflections from each phase are not well separated, neither the LeBail nor Rietveld based method is able to robustly extract lattice parameters from either phase. Unlike the vacancy-containing $K_xFe_{2-y}Se_2$ analogues,[16] there are no weak supercell peaks or other signs of additional structural periodicities. Quantitative refinement of the lattice parameters for single-phase products (using an internal standard) are summarized in Table 2. The high symmetry of $I4/mmm$ permits both the nearest-neighbor Ni−Ni distance $(a\sqrt{2}/2)$ and interlayer spacing $(c/2)$ to be extracted solely from the lattice parameters.

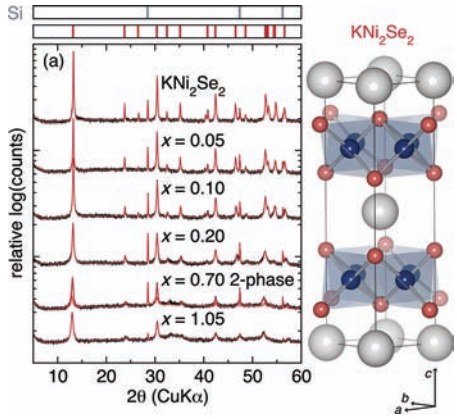

Figure 2. Rietveld analysis of X-ray diffraction data of KNi_2Se_2 and its oxidation products illustrates retention of the parent $I4/mmm$ symmetry of KNi_2Se_2 across the whole series, where x = mol $[Cu^{2+} + 2I^-]$/mol KNi_2Se_2. Note the logarithmic scale on the y axis used to indicate the absence of impurity phases. Hashes above the panels denote allowed reflection positions for KNi_2Se_2 and Si (internal standard). A schematic representation of the unit-cell is presented on the right (Ni = blue, Se = red, K = silver). The $ThCr_2Si_2$-type structure comprises tetrahedral $[Ni_2Se_2]^-$ layers of edge-sharing $[NiSe_4]$ tetrahedra separated by K^+ ions.

Table 2. Lattice Parameters of $K_{1-x}Ni_2Se_2$ and $K_{1-y}Ni_{2-z}Se_2$ Extracted from Rietveld Analysis with $I4/mmm$[a]

x[b]	compd	a (Å)	c (Å)
0	KNi_2Se_2	3.9098(8)	13.4142(5)
0.05	$K_{0.95}Ni_2Se_2$	3.9054(9)	13.4397(5)
0.1	$K_{0.9}Ni_2Se_2$	3.9018(1)	13.4679(6)
0.2	$K_{0.8}Ni_2Se_2$	3.8923(2)	13.5249(8)
1.05	$K_{0.37}Ni_{1.75}Se_2$	3.8476(4)	13.717(2)
2 (3 days)	$K_{0.37}Ni_{1.75}Se_2$	3.841(4)	13.71(1)
2 (8 days)	$K_{0.25}Ni_{1.5}Se_2$	3.872(5)	13.59(1)

[a]All lattice parameters reported from Rietveld analysis with an internal Si standard. [b]x = [mol $Cu^{2+} + 2I^-$]/mol KNi_2Se_2.

These parameters allow us to construct the phase diagram shown in Figure 3.

For compounds with $x < 0.25$, the structural parameters follow Végard behavior:[17] the Ni−Ni distance $(a\sqrt{2}/2)$ contracts linearly with x and the separation between layers expands linearly with x. Beyond the two-phase region, the distances no longer follow Végard behavior, as both potassium and nickel are removed from the lattice. For 3 day reactions at x = 1.05 and x = 2, the structural parameters are nearly identical. Reactions with x = 2 for 8 days inverts the observed trend, with the Ni−Ni distance expanding and the layer separation contracting. Rietveld analysis of synchrotron X-ray diffraction data acquired from the oxidation products (x = 0.05, 0.1, 0.2, 1.05) confirms these trends (Supporting Information and cif files). Refinement of the peak intensities confirms the expected composition and reveals that nickel atoms displace out of the $[Ni_2Se_2]$ layers and into the interlayer space to occupy the vacant K site with split-site occupancy.

Compositional analysis by inductively coupled plasma spectroscopy of select products resolves the details of the chemical reactivity (Table 3). The reaction with x = 0.1 selectively removes potassium with stoichiometric control. For $x > 1$, nickel is also removed from the lattice to yield

dx.doi.org/10.1021/ja212012k | J. Am. Chem. Soc. 2012, 134, 7750−7757

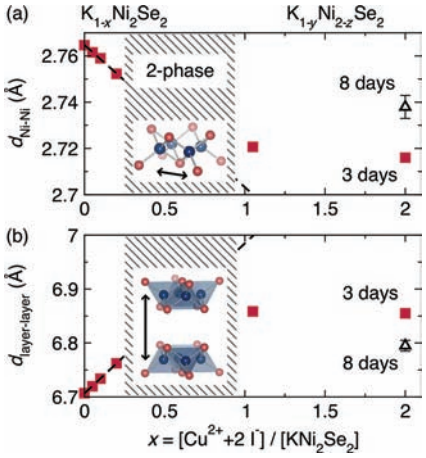

Figure 3. (a) Nearest-neighbor Ni−Ni distances and (b) interlayer separation from the tetragonal unit cell parameters ($d_{Ni-Ni} = a\sqrt{2}/2$, $d_{layer-layer} = c/2$) as a function of moles of oxidant, where x = mol $[Cu^{2+} + 2I^-]$/ mol KNi_2Se_2). The distances follow Végard behavior for $x \leq 0.2$ of $K_{1-x}Ni_2Se_2$ (insets). A two-phase region extends from $0.25 \leq x \leq 0.90$. Excess oxidation with $x \geq 1$ leads to nickel extraction, $K_{1-y}Ni_{2-z}Se_2$, causing increased intralayer Ni−Ni distances and collapsed layer-to-layer Ni−Ni distances compared to those expected from low x behavior. In the small insets, Ni = blue, Se = red.

Table 3. Sample Composition from ICP-OES[a]

	relative composition (moles)				
x^b	K	Ni	Se	K/Ni	no. electrons removed
0	0.92	1.91	2.00	0.96/2.00	
0.1	0.81	1.94	2.00	0.84/2.00	0.10
1.05	0.37	1.73	2.00	0.43/2.00	0.90
2	0.25	1.51	2.00	0.33/2.00	1.47

[a]ICP-OES (Inductively coupled plasma−optical emission spectroscopy). [b]x = mol $[Cu^{2+} + 2I^-]$/mol KNi_2Se_2

$K_{1-y}Ni_{2-z}Se_2$ with retention of the parent KNi_2Se_2 symmetry (Figure 2).

The magnetic properties of all the resulting compounds (Figure 4) are consistent with Pauli paramagnetic behavior; no superconductivity or magnetic phase transitions were observed down to T = 2 K. The extraction of potassium does not significantly alter the magnetic response of the materials, as expected for a Pauli paramagnet.

Reaction products with nickel vacancies, as in x = 1.05 ($K_{0.37}Ni_{1.75}Se_2$) or x = 2 ($K_{0.25}Ni_{1.5}Se_2$), are metastable, transforming slowly to a different structure, even at room temperature. Over the course of 66 days at room-temperature (297 K) in an inert atmosphere, $K_{0.25}Ni_{1.5}Se_2$ partially converts into a structure resembling Ni_3Se_4 ($I2/m$),[19] a vacancy-ordered version of the NiAs structure type (Figure 5). Despite the small crystalline coherence length of the Ni_3Se_4 phase, it comprises 85(15) mol % of the sample by Rietveld analysis. At elevated temperatures, the conversion rate rapidly increases: 15 min at 338 K yields 30(15) mol %, 10 min at 403 K yields 55(15) mol %, 5 min at 573 K yields complete conversion. These values represent the minimum conversion fraction based on appropriately weighted scale factors in Rietveld analysis or the absence of the (013) reflection of $K_{1-y}Ni_{2-z}Se_2$ ($2\theta \approx 30.5°$) used to indicate complete conversion.

These results outline two regimes of the oxidative deintercalation reactions separated by a two-phase region:

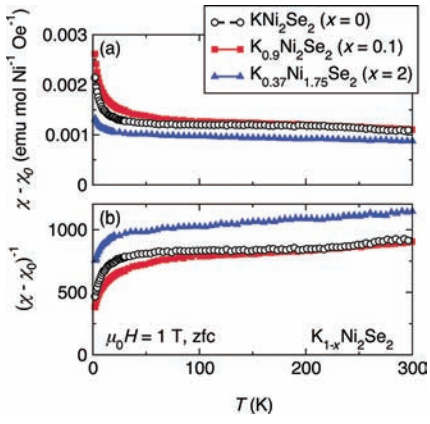

Figure 4. (a) Temperature dependence of the magnetic susceptibilities of KNi_2Se_2, $K_{0.9}Ni_2Se_2$, and $K_{0.37}Ni_{1.75}Se_2$ indicating temperature-independent Paul paramagnetic behavior. Data are corrected for temperature independent contributions (χ_0) attributed to the diamagnetic sample holder and parasitic ferromagnetic contributions.[18] (b) Inverse of the corrected magnetic susceptibility. Data collected on zero-field cooling with an applied field of μ_0H = 1 T.

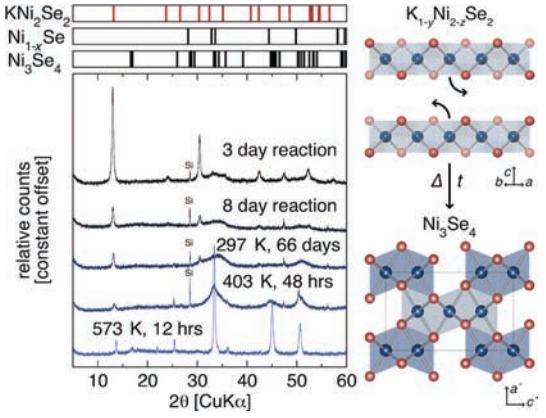

Figure 5. X-ray diffraction data illustrating the metastability of the fully oxidized product (x = 2), and the spontaneous transformation into Ni_3Se_4 (vacancy-ordered NiAs structure) over time (66 days) or at elevated temperature (403 K, 573 K). The peak positions of the internal standard Si are marked. Right: Illustrated transformation of $K_{1-y}Ni_{2-z}Se_2$ (top) into Ni_3Se_4 (bottom) from the displacement of nickel atoms into the interlayer space.

low oxidant concentrations ($x \leq 0.25$), when potassium extraction accompanies oxidation, and high oxidant concentrations ($x \geq 1$), when both potassium and nickel extraction accompany oxidation. To gain further insight in these reactions and transformations, we determined the activation barriers for the average rate-limiting steps in the extraction of potassium (Figure 6a) and the phase transformation from $K_{1-y}Ni_{2-z}Se_2$ into Ni_3Se_4 (Figure 6b).

The rates of potassium deintercalation were determined by the time-to-completion of solution reactions targeting x = 0.2 as a function of reaction temperature (296, 316, 333, and 355 K). The time required for the solution to turn clear from brown/amber enables the estimation of an average rate constant of the overall reaction (k_{avg}). Assuming zeroeth-order reaction kinetics, the activation barrier for the rate-limiting step was estimated from the Arrhenius relationship, $\ln(k_{avg}) = -\Delta G^{\ddagger}/(RT) + \ln(k_0)$, where $\Delta G^{\ddagger}$ = 0.20(3) eV. A similar analysis (not shown) assuming first or second-order kinetics gives the same

dx.doi.org/10.1021/ja212012k | J. Am. Chem. Soc. 2012, 134, 7750−7757

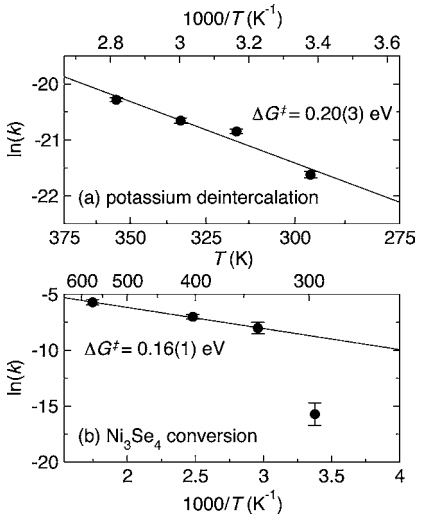

Figure 6. Arrhenius temperature dependence of the zeroeth-order average rate constant (k), linearized as the natural logarithm [$\ln(k_{avg})$] as a function of the inverse reaction temperature [$1000/T$], $\ln(k_{avg}) = -\Delta G^{\ddagger}/(RT) + \ln(k_0)$, to estimate an activation barrier for the rate-limiting steps of (a) solid-state diffusion of K^+ in the deintercalation reaction, $\Delta G^{\ddagger} = 0.20(3)$ eV, and (b) nucleation and growth of the structural conversion to Ni_3Se_4, with a maximum limit to the activation energy for growth of $\Delta G^{\ddagger} = 0.16(1)$ eV.

result. Furthermore, the logarithmic dependence of k_{avg} on $\Delta G^{\ddagger}$ makes this analysis insensitive to errors in measuring k_{avg} or k_0. Thus, this is a robust and general approach to estimating the overall rate-limiting process.

The kinetics of the $K_{1-y}Ni_{2-z}Se_2$ to Ni_3Se_4 phase transformation were studied in a similar manner. The phase fraction converted was monitored as a function of time and temperature. An effective average rate constant was estimated from the fraction converted after a given time at each temperature. For the solid–solid transformation, the $\ln(k_{avg})$ values at each temperature are collinear with T^{-1} at $T \gtrsim 330$ K with low effective activation energy, carrying a maximum bound of $\Delta G^{\ddagger} = 0.16(1)$ eV. The reaction still occurs at $T = 296$ K, but at a rate significantly slower than expected from the elevated-temperature reactions. Taken together, these results indicate multiple reaction barriers to potassium and nickel extraction and the structural phase transformation from $ThCr_2Si_2$-type to NiAs-type structures, as discussed below with respect to their origins arising from Ni–Ni bonding.

DISCUSSION

At low oxidant concentrations ($x \leq 0.20$), the oxidative deintercalation of KNi_2Se_2 to $K_{1-x}Ni_2Se_2$ with Cu^{2+} and $2I^-$ has explicitly separated oxidation and deintercalation reactions:

$$KNi_2Se_{2(s)} + x[Ox] + x[DInt] \rightleftharpoons K_{1-x}Ni_2Se_{2(s)} + xK[DInt] + x[Red] \quad (1)$$

with oxidation accomplished by Cu^{2+} ([Ox] = Cu^{2+}, [Red] = Cu^+) and deintercalation driven by I^- ([DInt] = $2I^-$). To properly describe the defects in solid KNi_2Se_2 in this equilibrium equation, we rewrite the reaction in Kröger-Vink notation,

$$xK_K^{\times} + xNi_{Ni}^{\times} + xCu^{2+} \rightleftharpoons xVa'_K + xNi_{Ni}^{\bullet} + xK^+ + xCu^+ \quad (2)$$

where $K_K^{\times}$ is a neutrally charged potassium atom on a potassium site and Va'_K is a negatively charged potassium site vacancy. Likewise, $Ni_{Ni}^{\times}$ describes a neutrally charged nickel atom on a nickel site and $Ni_{Ni}^{\bullet}$ is a hole residing on a nickel site. The other species are in solution. Charges must balance, both within the overall reaction and between components within the solution alone and within the solid alone.

This notation allows explicit delineation of the oxidation and deintercalation reactions, respectively:

$$Ni_{Ni}^{\times} \rightarrow Ni_{Ni}^{\bullet} + e^- \quad (3)$$

$$K_K^{\times} \rightarrow Va'_K + K^+ \quad (4)$$

The copper redox couple provides an electrochemical potential to ensure spontaneity of the oxidation reaction (eq 3), while I^- provides a strong thermodynamic driving force for the extraction of K^+ and the overall reaction by way of KI formation.

The systematic introduction of holes into the nickel sublattice explains the linear contraction of the Ni–Ni distances with increasing oxidation (Figure 3a). This result is consistent with the displacement of nickel atoms from the ideal site into the interlayer space, garnered from Rietveld analysis of the synchrotron X-ray diffraction data. Additionally, the result is consistent with the formal oxidation from $Ni^{1.5+}$ to Ni^{2+}, which has a smaller ionic radius. Correspondingly, the removal of potassium results in an increased interlayer separation (Figure 3a) due to decreased electrostatic screening between negatively charged layers, as expected.[6]

The experimentally determined activation barrier for $x = 0.2$, $\Delta G^{\ddagger} = 0.20(3)$ eV (Figure 6), is consistent with the diffusion of alkali metal ions in layered compounds.[20−22] Thus, we infer that kinetic control is achieved by the deintercalation rate of $K_K^{\times}$ (eq 4), and that the solid-state diffusion of K^+ is the rate-limiting step for the overall reaction when $x \leq 0.20$.

At high oxidant concentrations ($x > 0.9$), a second ion extraction reaction occurs in parallel with K^+ removal. Both compositional analysis (Table 3) and Rietveld analysis (Figure 3) indicate that the products for $x > 0.9$ are nickel deficient. From this, we infer that the formation energy of additional Va'_K species becomes similar to that of removing nickel, that is, nickel vacancy (Va'_{Ni}) by the reaction,

$$2Ni_{Ni}^{\times} + 2Cu^{2+} \rightleftharpoons Va'_{Ni} + Ni_{Ni}^{\bullet} + Ni^{2+} + 2Cu^+ \quad (5)$$

This secondary process explains the different structure parameters for $x = 2$, when reacted at 3 days versus 8 days (Figure 3). The defect formation energy can determine the rate by which the reaction occurs. Considering the low activation barrier for potassium deintercalation at room temperature, the inclusion of this additional reaction pathway is not immediately obvious from the perspective of kinetics. We hypothesize that this alternate oxidation reaction (eq 5) is a direct consequence of electron count and bonding within the $[Ni_2Se_2]$ layers.

Hoffmann and Zheng previously used molecular-orbital diagrams to describe trends in bonding in $ThCr_2Si_2$-type structures, with a specific focus on dimerization of the anions between layers.[23,24] Figure 7a illustrates a schematic molecular orbital (MO) diagram of direct Ni–Ni bonding orbitals in a $[Ni_2Se_6]$ dimer of edge-sharing $[NiSe_4]$ tetrahedra. The dimer

dx.doi.org/10.1021/ja212012k | J. Am. Chem. Soc. 2012, 134, 7750−7757

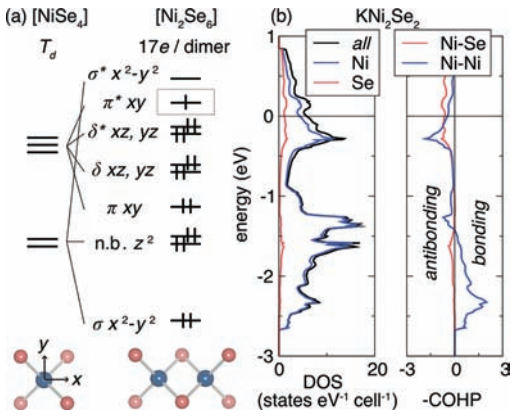

Figure 7. (a) Schematic molecular orbital diagram of Ni−Ni bonding orbitals, illustrated by the dimerization of a $[NiSe_4]$ tetrahedral crystal field (left), resulting in 10 distinct molecular orbitals (three doubly degenerate) for a $[Ni_2Se_6]$ dimer. (b) The electronic densities-of-states (DOS) from a TB-LMTO-ASA calculation of KNi_2Se_2 qualitatively corresponds to the dispersion of the Ni−Ni bonding orbitals of the dimer into bands. Formally, KNi_2Se_2 has $17e^-$/dimer. From either perspective (molecular dimer or extended solid), removal of one electron depopulates an antibonding π^* orbital an antibonding band (COHP) to yield shorter Ni−Ni bond lengths (a axis contraction).

presents a more realistic layer building block as it includes the direct Ni−Ni bonding omitted in an isolated T_d crystal field. Construction of the $[Ni_2Se_6]$ dimer starts with Ni 3d orbitals from an ideal $[NiSe_4]$ tetrahedral crystal field. The crystal-field split atomic orbitals then disperse into 10 distinct molecular orbitals of the dimer, three of which are degenerate.

The nature of the Ni−Ni bonding molecular orbitals, with partial contributions from the ligands, are labeled by the atomic 3d orbitals and overlap (σ, π, δ, and nonbonding) in Figure 7a. With the crystal-field x (or y) axes aligned with adjacent Ni atoms, the atomic $d_{x^2-y^2}$ orbitals widely disperse in energy to create σ bonding and σ^* antibonding Ni−Ni molecular orbitals. The d_{z^2} orbitals are nonbonding. From the t_2 set, the d_{xz} and d_{yz} orbitals weakly overlap in the dimer, resulting in little dispersion of the δ and δ^* orbitals. The d_{xy} orbitals form moderately dispersed π and π^* orbitals.

In the solid, these discrete energy levels disperse and delocalize into bands, with bandwidths and energy−momentum relationships relating to orbital overlap (geometry, polarizability) and symmetry (parity).[23] The molecular orbital diagram is not provided to imply explicit dimerization in the solid, but rather to qualitatively describe the direct interactions between adjacent Ni atoms. A density-functional theory (DFT) calculation of the electronic structure of KNi_2Se_2 qualitatively takes a similar shape as the $[Ni_2Se_6]$ molecular orbitals (Figure 7). Thus, we consider the molecular orbitals as a valid proxy for understanding bonding in the extended lattice, a concept well established by Hoffmann.[23] The propagation of the molecular orbitals across the Brillouin zone results in dispersed bands at the top and bottom of the densities-of-states (DOS) corresponding to the σ and σ^* $d_{x^2-y^2}$ orbitals; localized nonbonding states appear at the same relative position the nonbonding d_{z^2} orbitals.

By formal electron count with 2 $Ni^{1.5+}$ ions, there are 17 electrons per dimer, resulting in half-filling of the highest occupied π^* antibonding molecular orbital, or location of the Fermi energy within bands of antibonding character. By this model, oxidation depopulates the antibonding π^* orbital and increases the Ni−Ni bond-order, in agreement with the observed contraction between intralayer Ni atoms (Figure 3). Furthermore, this model explains the expansion of M−M distances observed crossing the periodic table from KCo_2Se_2 (d_{Co-Co} = 2.73 Å)[15] to KNi_2Se_2 (d_{Ni-Ni} = 2.76 Å), to KCu_2Se_2 (orthorhombic $Fmmm$, d_{Cu-Cu} = 2.83 and 2.84 Å);[25] this is the opposite trend to what is expected from trends in atomic sizes of M. As the number of electrons is increased from $15e^-$/$[Co_2Se_6]$ dimer to $17e^-$/$[Ni_2Se_6]$ dimer to $19e^-$/$[Cu_2Se_6]$ dimer, they increasingly fill antibonding M−M orbitals. For KCu_2Se_2, a half-filled σ^* $d_{x^2-y^2}$ orbital is electronically unstable; this degeneracy is relieved by "breaking" one dimer with a small orthorhombic distortion, as experimentally observed.[25]

This direct Ni−Ni bonding offers an electronic driving force for Va'_{Ni} formation, providing nickel mobility. Our data indicate that nickel is relatively mobile in $K_{1-y}Ni_{2-z}Se_2$ at room temperature (Table 3). Nickel vacancy formation progresses with time, considering x = 2 at 3 days versus 8 days: the increased reaction time brings about an increase in the average Ni−Ni distance (Figure 3), consistent with the reduced electrostatic screening between anion ligands.[26] We speculate that as the average nickel oxidation state approaches Ni^{2+}, the electronic stabilization afforded by the increased Ni−Ni bond-order of oxidized nickel sites (dimerization) reduces the activation barrier for nickel vacancy formation on neutral nickel sites. Alternatively, the removal of potassium reduces the nickel oxidation potential, facilitating its removal (eq 5) by way of the inductive effect.[27] While dimerization of the nickel atoms is not immediately observed, the decomposition of metastable $K_{1-y}Ni_{2-z}Se_2$ into a NiAs-type structure supports this hypothesis.

As illustrated in Figure 5, $K_{1-y}Ni_{2-z}Se_2$ slowly converts at room-temperature to Ni_3Se_4, a vacancy-ordered variation of the hexagonal NiAs structure. This transformation begins even for x < 0.2, as we observe the displacement of nickel from its ideal position into the interlayer space using synchrotron X-ray diffraction. This is related to conversion of $Fe_{1.01}Se$ from the anti-PbO structure to NiAs structure at high pressure (P > 30 GPa).[28] We find that there is a low-energy pathway linking these two phases; the distinct nickel coordination polyhedra of the two phases (tetrahedral versus octahedral) disguises their close structural relationship. The schematic representation of the structures in Figure 5 along $\langle a_{tet}\ b_{tet}\ 0\rangle$ and $\langle 0\ b'\ 0\rangle$ (the prime indicates the unit-cell indices of the Ni_3Se_4 phase) illustrates the distinct coordination polyhedra. In this orientation, both phases have the same registry between adjacent nickel atoms within a layer. The filling of the interlayer space by mobile Ni atoms, indicated by the curved arrow in Figure 5, initializes the phase transformation of $K_{1-y}Ni_{2-z}Se_2$ into Ni_3Se_4. The vacancy-ordered Ni_3Se_4 structure is a monoclinic supercell of the canonical hexagonal NiAs structure type with a shared c_{hex} axis.

The displacive phase transition is illustrated in Figure 8. Looking down on a $\{0\ 0\ l_{tet}\}$ layer of $K_{1-y}Ni_{2-z}Se_2$ along $\langle 0\ 0\ l_{tet}\rangle$ reveals the square network of Ni and Se atoms in a $[Ni_{2-z}Se_2]$ layer (Figure 8). Conversion to the hexagonal NiAs structure type requires displacement of the Se atoms along $\langle h_{tet}\ h_{tet}\ 0\rangle$ crystal directions, accompanied by a slight elongation. This direction is equivalent to the hexagonal $\langle 2h_{hex}\ k_{hex}\ 0\rangle$ crystal directions in the NiAs structure. To generate the hexagonal closest-packing of the NiAs structure, one needs only to select one $\{h_{tet}\ h_{tet}\ 0\}$ plane from the tetragonal structure (indicated by the dashed gray box in Figure 8) and orient the

dx.doi.org/10.1021/ja212012k | J. Am. Chem. Soc. 2012, 134, 7750−7757

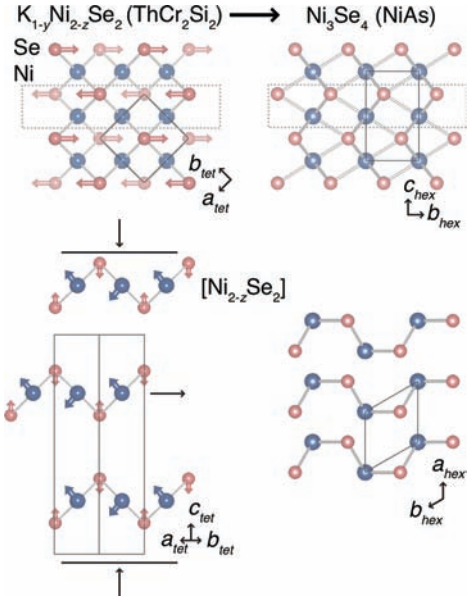

Figure 8. Displacive structural transformation from metastable $K_{1-y}Ni_{2-z}Se_2$ into Ni_3Se_4 (vacancy-ordered NiAs structure) illustrating (top) displacements of Se atoms relative to the Ni atoms viewed along the tetragonal $\langle 0\ 0\ l_{tet}\rangle$ direction. The dashed box illustrates a slice along a tetragonal $\{h_{tet}\ h_{tet}\ 0\}$ plane, which forms the closest-packed hexagonal $\{0\ 0\ l_{hex}\}$ planes of the NiAs structure. The formation of the hexagonal closest-packed planes (bottom) occurs via collapse and shift (indicated by black arrows) of the tetragonal $\{0\ 0\ l_{tet}\}$ $[Ni_{2-z}Se_2]$ planes with displacements of the Ni atoms along the $\langle 2h_{tet} - 2h_{tet} \pm l_{tet}\rangle$ directions and of the Se atoms along the $\langle 0\ 0 \pm l_{tet}\rangle$ directions. Ni atoms are represented in blue, Se atoms in red; projection of the tetragonal and hexagonal unit-cells are denoted by boxes.

slice along the $\langle h_{tet}\ h_{tet}\ 0\rangle$ direction (Figure 8, bottom). This orientation is equivalent to the hexagonal $\langle 0\ 0\ l_{hex}\rangle$ crystal directions in the NiAs structure. Within each $[Ni_{2-z}Se_2]$ layer are displacements of the Ni atoms along the $\langle 2h_{tet} - 2h_{tet} \pm l_{tet}\rangle$ directions and of the Se atoms along the $\langle 0\ 0 \pm l_{tet}\rangle$ direction (Figure 8, bottom left). These projected layers collapse along $\langle 0\ 0\ l_{tet}\rangle$ and shift along $\langle h_{tet}\ h_{tet}\ 0\rangle$ to produce the hexagonal closest-packed layers of the hexagonal NiAs structure type.

Along with the structural phase transformation comes a contraction of the Se−Se distances: 3.9 Å in KNi_2Se_2 versus 3.3 Å in Ni_3Se_4.[19] By formal electron count in $K_{0.25}Ni_{1.5}Se_2$, nickel has an unreasonably high formal oxidation state of $Ni^{2.5+}$. Rather than the formal oxidation of nickel, the formal oxidation of selenium and formation of delocalized Se−Se bonding states seems more likely in light of these bond distances and thermodynamically favorable oxidation of Se^{2-}.[29] This structural phase transformation requires only displacements of atoms rather than bond-breaking, thus providing a continuous low-energy pathway connecting the structures. The transformation to the NiAs-type structure results in the formation of additional bonds (2 additional Ni−Se bonds/Ni atom) and localization of Ni−Ni bonds.

Additionally, the close structural relationship offers an explanation for the kinetics of the phase transformation. At elevated temperature ($T \geq 338$ K), the transformation occurs rapidly. From an Arrhenius temperature dependence of the effective rate constant with temperature, the maximum bound for the activation barrier is $\Delta G^{\ddagger} = 0.16(1)$ eV. The close displacive structural relationship between the two structures without energetically unfavorable structural intermediates rationalizes this low activation barrier. However, the effective conversion rate at room-temperature is relatively very slow. We speculate that the conversion is dominated by nucleation and growth kinetics, in which the effective activation energy for transformation is temperature dependent.[30] In this case, the activation energy for growth is low, but the concerted diffusion required for nucleation exhibits a higher effective activation energy.

■ CONCLUSIONS

These results have broad implications in battery materials, superconductors, and *chimie douce* reactions. The kinetic mechanisms and competing reactions are related to those found in traditional battery materials, such as $LiCoO_2$, and may be an origin of undesirable two-phase regions.[6] The low activation energy for nickel vacancy formation and high nickel mobility provides chemical insight behind the controversial relationships of vacancy-order and the emergence of magnetism or superconductivity in iron selenide compounds, $A_{1-y}Fe_{2-z}Se_2$.[16,31−36] Furthermore, the low-energy pathway for conversion from a $ThCr_2Si_2$-type layer to the NiAs-type structures suggests a need for rigorous characterization, even in single-crystal samples,[37] both before and after measurements of the physical properties owing to the non-negligible mobility of both alkali and transition metals at room temperature. Additionally, a complex composition/structure/property relationship exists with $K_{1-x}Ni_2Se_2$ and $K_{1-y}Ni_{2-z}Se_2$ and warrants further focused attention with regard to precise details of the reaction mechanisms and of the local structure to look for dimerization.

■ EXPERIMENTAL SECTION

All starting elements and reagents were purchased from either Sigma-Aldrich or Alfa Aesar with purity levels > 98%. KNi_2Se_2 was prepared from the elements involving prereaction of Ni foil and Se shot at 723 K for 12 h in an evacuated quartz ampule (<10 mTorr) with a carbon getterer, physically separated by a neck in the ampule;[38] the product was then melted at 1323 K and slowly cooled to yield $NiSe_{1+\delta} + \delta Ni$.[39] Then, 51 mol % of K was added to the mixture and prereacted as a loose powder at 723 K (at 75 K/h, 6 h) followed by pelletization and heating at 1023 K (at 125 K/h, held for 72 h, followed by a water quench) in double-sealed quartz ampules to yield bright red/purple, lustrous pellets.[15] X-ray diffraction (XRD) patterns of powders intimately mixed with Si were collected on a Bruker D8 Focus instrument using monochromatic Cu Kα X-rays and an energy-discriminating LynxEye detector. Powders were immobilized onto glass slides with petroleum jelly and were immediately diffracted using 4 min scans to avoid their decomposition in air. Scans recorded hours later revealed significant decomposition. Lattice parameters were extracted by LeBail refinements to the XRD data using TOPAS (Bruker AXS), calibrated internally with Si (a = 5.143102 Å);[40] Rietveld analyses were conducted in the same manner. Synchrotron X-ray diffraction data of KNi_2Se_2 were collected on beamline 11-BM (KNi_2Se_2) and beamline 11-ID-B ($K_{1-x}Ni_2Se_2$) at the Advanced Photon Source, Argonne National Laboratory.[41] Structural refinements of the synchrotron XRD data were conducted using EXPGUI/GSAS[42,43] initialized with the previously reported structural model.[15] Structures were visualized using VESTA.[44]

All data presented on $K_{1-x}Ni_2Se_2$ came from the same batch of KNi_2Se_2. Stoichiometric oxidation reactions followed eq 1 with Cu^{2+}+ $2I^-$ in a Schlenk flask using air-free techniques. Different reactions targeted x = 0.05, 0.1, 0.2, 0.25, 0.3, 0.5, 0.6, 0.75, 0.8, 0.9, and 1.05, where x = mol $[Cu^{2+}+ 2I^-]$/mol KNi_2Se_2, in 100−200 mg batches, with 100 mg of KNi_2Se_2/6 mL of solution. Stock solutions of 0.1 M $Cu^{2+}+ 2I^-$ were prepared by dissolving stoichiometric amounts of dry CuI and $0.5I_2$ into deoxygenated (via N_2 bubbling) and dehydrated

dx.doi.org/10.1021/ja212012k | J. Am. Chem. Soc. 2012, 134, 7750−7757

(molecular sieves with 3 Å pores) acetonitrile. As Cu^{2+}+ $2I^-$ is strongly brown/amber in color and Cu^++ I^- is clear, the reactions were stirred at 297 K until there was no change in the solution color (~24−96 h). Powders were settled, decanted, and rinsed 5× with acetonitrile and dried in vacuo at 297 K before harvesting in an argon filled glovebox. Compositions of the reaction products were determined using inductively coupled plasma optical emission spectroscopy (ICP-OES) by Huffman Laboratories, Golden, CO, with handling of all samples in dry environments before digestion into appropriate solutions.

Kinetic studies targeted $K_{0.8}Ni_2Se_2$ using 0.2 mol equiv of Cu^{2+}+ $2I^-$ at different temperatures, T = 297, 316, 333, and 355 K. The total reaction time was noted by transparency of the supernatant. The time to completion was used to calculate an effective zeroeth-order rate constant for the average rate-limiting step of the reaction to calculate the activation energy, $\Delta G^{\ddagger}$.

The temperature-dependent metastability of $K_{1-y}Ni_{2-z}Se_2$ was tested by pelletization of the oxidized powders and sealing in evacuated quartz ampules. The ampules were then heated in furnaces at 338 K (15 min), 403 K (10 min, 2 h, and 48 h), and 573 K (5 min, 1 h, and 12 h). The products were opened to air and immediately X-ray diffraction was performed.

Temperature dependence of the magnetization were measured from 2 to 300 K on powders immobilized and sealed in $C_{20}H_{42}$ wax in polycarbonate capsules in a argon filled glovebox. Measurements were performed using the ACMS options on a Physical Properties Measurement System (Quantum Design, Inc.) measuring the zero-field cooled and field cooled magnetization at $\mu_0 H$ = 1 T. Diamagnetic contributions from the sample holder were measured and subtracted. Parasitic ferromagnetic contributions at 300 K, determined using the method described by Honda,[18] were also subtracted.

Electronic structures were calculated using the STUTTGART TB-LMTO-ASA program[45] using an input structure of KNi_2Se_2 obtained from Rietveld refinement of XRD data. The exchange-correlation potential of the density function theory (DFT) is described within the local density approximation (LDA) using more than 150 irreducible k points in the Brillouin zone. The calculations provided the overall electronic densities-of-states and their decomposition into individual contributions from Ni and Se. Insight into bonding is provided through the crystal orbital Hamiltonian populations (COHPs), where positive values of −COHP designate bonding states and negative values of −COHP are antibonding states.[46] The calculations serve as a qualitative propagation of electronic bands extended from molecular orbitals of discrete molecular building blocks, rather than an exacting calculation of the electronic structure.

■ ASSOCIATED CONTENT

Supporting Information

Synchrotron X-ray diffraction data and Rietveld analysis with cif files. This material is available free of charge via the Internet at http://pubs.acs.org.

■ AUTHOR INFORMATION

Corresponding Author

mcqueen@jhu.edu

Notes

The authors declare no competing financial interest.

■ ACKNOWLEDGMENTS

The authors thank Dr. Anna Llobet for assistance with collection of the synchrotron X-ray diffraction data. This research was supported by The Institute for Quantum Matter, funded by the U.S. Department of Energy, Office of Basic Energy Sciences, Division of Materials Sciences and Engineering under Award DE-FG02-08ER46544. This research has benefited from the use of beamline 11-BM and beamline 11-ID-B at the Advanced Photon Source at Argonne National Laboratory, supported by the U.S. Department of Energy, Office of Science, Office of Basic Energy Sciences, under Contract No. DE-AC02-06CH11357.

■ REFERENCES

(1) Mizushima, K.; Jones, P.; Wiseman, P.; Goodenough, J. *Mater. Res. Bull.* **1980**, *15*, 783−789.
(2) Tarascon, J. *Nature* **2008**, *451*, 652−657.
(3) Rouxel, J.; Tournoux, M. *Solid State Ionics* **1996**, *84*, 141−149.
(4) Schollhorn, R. *Angew. Chem., Int. Ed.* **1988**, *27*, 1392−1400.
(5) Schleich, D. *Solid State Ionics* **1994**, *70/71*, 407−411.
(6) Hertz, J.; Huang, Q.; McQueen, T.; Klimczuk, T.; Bos, J. W. G.; Viciu, L.; Cava, R. J. *Phys. Rev. B* **2008**, *77*, 075119.
(7) Murphy, D.; Carides, J.; Salvo, F. D.; Cros, C.; Waszczak, J. *Mater. Res. Bull.* **1977**, *12*, 825−830.
(8) Bruggen, C. V.; Haange, R.; Wiegers, G.; Boer, D. D. *Phys. B+C* **1980**, *99*, 166−172.
(9) Takada, K.; Sakurai, H.; Takayama-Muromachi, E.; Izumi, F.; Dilanian, R. A.; Sasaki, T. *Nature* **2003**, *422*, 53−55.
(10) Gocke, E.; Schoellhorn, R.; Aselmann, G.; Mueller-Warmuth, W. *Inorg. Chem.* **1987**, *26*, 1805−1812.
(11) Potel, M.; Gongeon, P.; Chevrel, R.; Sergent, M. *Rev. Chim. Miner.* **1984**, *21*, 509.
(12) Tarascon, J. M.; Murphy, D. W. *Phys. Rev. B* **1986**, *33*, 2625−2635.
(13) ter Haar, L. W.; Di Salvo, F. J.; Tarascon, J. M. *Phys. Rev. B* **1986**, *34*, 7342−7349.
(14) Hughbanks, T.; Hoffmann, R. *J. Am. Chem. Soc.* **1983**, *105*, 1150−1162.
(15) Huan, G.; Greenblatt, M.; Croft, M. *Eur. J. Solid State Inorg. Chem.* **1989**, *26*, 193−220.
(16) Bacsa, J.; Ganin, A. Y.; Takabayashi, Y.; Christensen, K. E.; Prassides, K.; Rosseinsky, M. J.; Claridge, J. B. *Chem. Sci.* **2011**, *2*, 1054−1058.
(17) Vegard, L. *Z. Phys. A: Hadrons Nucl.* **1921**, *5*, 17−26.
(18) Honda, K. *Ann. Phys.* **1910**, *337*, 1027−1063.
(19) Hiller, J. E.; Wegener, W. *Neues Jahrb. Mineral.* **1960**, *94*, 1147−1159.
(20) England, W. A.; Goodenough, J. B.; Wiseman, P. J. *J. Solid State Chem.* **1983**, *49*, 289−299.
(21) Van der Ven, A.; Thomas, J. C.; Xu, Q.; Swoboda, B.; Morgan, D. *Phys. Rev. B* **2008**, *78*, 104306.
(22) Kang, K.; Ceder, G. *Phys. Rev. B* **2006**, *74*, 094105.
(23) Hoffmann, R. *Solids and Surfaces: A Chemist's View of Bonding in Extended Structures*; VCH: New York, 1988.
(24) Hoffmann, R.; Zheng, C. *J. Phys. Chem.* **1985**, *89*, 4175−4181.
(25) Tiedje, O.; Krasovskii, E. E.; Schattke, W.; Stoll, P.; Näther, C.; Bensch, W. *Phys. Rev. B* **2003**, *67*, 134105.
(26) Neilson, J. R.; Kurzman, J. A.; Seshadri, R.; Morse, D. E. *Chem.—Eur. J.* **2010**, *16*, 9998−10006.
(27) Tarascon, J.-M. *Nature* **2001**, *414*, 359−367.
(28) Medvedev, S.; McQueen, T. M.; Troyan, I.; Palasyuk, T.; Eremets, M. I.; Cava, R. J.; Naghavi, S.; Casper, F.; Ksenofontov, V.; Wortmann, G.; Felser, C. *Nat. Mater.* **2009**, *8*, 630−633.
(29) Vanýsek, P. Electrochemical Series. In *CRC Handbook of Chemistry and Physics*, 87th ed.; Lide, D., Ed.; Taylor and Francis: New York, 2005; pp 1−10.
(30) Liu, F.; Sommer, F.; Bos, C.; Mittemeijer, E. *Int. Mater. Rev.* **2007**, *52*, 193−212.
(31) Guo, J.; Jin, S.; Wang, G.; Wang, S.; Zhu, K.; Zhou, T.; He, M.; Chen, X. *Phys. Rev. B* **2010**, *82*, 180520.
(32) Li, W.; Ding, H.; Deng, P.; Chang, K.; Song, C.; He, K.; Wang, L.; Ma, X.; Hu, J.-P.; Chen, X.; Xue, Q.-K. *Nat. Phys.* **2011**, *7*, 1−5.
(33) Liu, R.; Luo, X.; Zhang, M.; Wang, A.; Ying, J.; Wang, X.; Yan, Y.; Xiang, Z.; Cheng, P.; Ye, G. *Europhys. Lett.* **2011**, *94*, 27008.
(34) Ye, F.; Chi, S.; Bao, W.; Wang, X.; Ying, J.; Chen, X.; Wang, H.; Dong, C.; Fang, M. *Phys. Rev. Lett.* **2011**, *107*, 137003.

(35) Yu, V.; Pomjakushin, V.; Sheptyakov, D. V.; Pomjakushina, E. V.; Krzton-Maziopa, A.; Conder, K.; Chernyshov, D.; Svitlyk, V.; Shermadini, Z. *Phys. Rev. B* **2011**, *83*, 144410.
(36) Zavalij, P.; Bao, W.; Wang, X. F.; Ying, J.; Chen, X. H.; Wang, D. M.; He, J. B.; Wang, X. Q.; Chen, G. F.; Hsieh, P.-Y.; Huang, Q.; Green, M. A. *Phys. Rev. B* **2011**, *83*, 132509.
(37) Hu, H.; Zuo, J.-M.; Wen, J.; Xu, Z.; Lin, Z.; Li, Q.; Gu, G.; Park, W. K.; Greene, L. H. *New J. Phys.* **2011**, *13*, 053031.
(38) Williams, A. J.; McQueen, T. M.; Cava, R. J. *Solid State Commun.* **2009**, *149*, 1507−1509.
(39) Lee, S. Y.; Nash, P. *Binary Alloy Phase Diagrams*, 2nd ed.; ASM International: Materials Park, OH, 1990.
(40) Massa, E.; Mana, G.; Kuetgens, U.; Ferroglio, L. *New J. Phys.* **2009**, *11*, 053013.
(41) Wang, J.; Toby, B. H.; Lee, P. L.; Ribaud, L.; Antao, S. M.; Kurtz, C.; Ramanathan, M.; Dreele, R. B. V.; Beno, M. A. *Rev. Sci. Instrum.* **2008**, *79*, 085105.
(42) Toby, B. H. *J. Appl. Crystallogr.* **2001**, *34*, 210−213.
(43) Larson, A. C.; Dreele, R. B. V. *Los Alamos Natl. Lab., [Rep.] LA (U.S)* **2000**, *86*, 748.
(44) Momma, K.; Izumi, F. *J. Appl. Crystallogr.* **2008**, *41*, 653−658.
(45) Krier, G.; Jepsen, O.; Burkhardt, A.; Andersen, O. K. *TB-LMTO-ASA47, MPI für Festkörperforschung*; Stuttgart: Germany, 1996.
(46) Dronskowski, R. *Adv. Solid State Phys.* **2002**, 433−444.